POLITECNICO DI TORINO
Repository ISTITUZIONALE

Commissioning and Sensorless Control of High Power SyR Machine Prototypes

Original
Commissioning and Sensorless Control of High Power SyR Machine Prototypes / Pescetto, P., Pellegrino, G., Armando, E.G.. - (2019). (2019 IEEE International Symposium on Sensorless Control for Electrical Drives (SLED) Torino) [10.1109/SLED.2019.8896265].

Availability:
This version is available at: 11583/2738592 since: 2020-01-29T09:39:07Z

Publisher:
IEEE

Published
DOI:10.1109/SLED.2019.8896265

Terms of use:

This article is made available under terms and conditions as specified in the corresponding bibliographic description in the repository

Publisher copyright

(Article begins on next page)

07 October 2026

Commissioning and Sensorless Control of High Power SyR Machine Prototypes

Paolo Pescetto, Eric Armando and Gianmario Pellegrino
Politecnico di Torino, Department of Energy "Galileo Ferraris", Torino, Italy
paolo.pescetto@polito.it

***Abstract*—This work deals with parameters identification of high power/ high current prototype of synchronous reluctance motor (250 kW). Both the converter and motor parameters are retrieved in a complete commissioning procedure. The obtained parameters are adopted for implementing a proper sensorless control strategy. The relevant size of the drive imposes several implementation issues and constrains, including the low switching frequency, that must be taken into account. Moreover, the machine presents very high harmonic distortion, deeply affecting the control.**

***Index Terms*—Synchronous reluctance machines, magnetic model identification, inverter commissioning, sensorless control, high current prototype.**

I. Introduction

Synchronous Reluctance Motors (SyRM) are becoming an interesting solution for critical high power applications thanks to their high efficiency, robustness and reliability, including More Electric Aircraft (MEA) [1]. In this contest, this work deals with a SyR prototype, called SR250kW, designed as starter generator for aerospace applications.

The relevance of this work is related to the high power rating of the machine under test, having a continuous power rating of 250 kW at 12.500 rpm, and a nominal phase current of 800 A rms. Such high power/current rating imposes several specific challenges. First of all, the the machine impedance is very low. The stator resistance is similar to the ON resistance of the inverter power modules (few $m\Omega$), and the phase inductance is in the order of magnitude of 10 mH. This leads to relevant risk of current control loss in case of inaccurate applied voltage. Second, the rating of the power converter IGBTs (2800 A pk, including machine overload) imposes a significant voltage error (circa 10 V), greater than the stator resistance voltage. Moreover, the voltage drop across the IGBTs is nonlinear up to relevant current (more than 200 A). Altogether, all these factors impose that a precise compensation of inverter non-linear effects is necessary for proper current and motor control.

The knowledge of the current-to-flux relationship, often called flux maps, is mandatory for most of the high performance control strategies. Machines of this current and power size are always custom designed, but the testing procedure is often problematic. The standard flux maps measurement techniques, such as [2], require a prime mover having a rated power higher or equal to the motor under test, which may not be available or not be practical. In this work, the flux maps were retrieved from self-commissioning tests [3] for 1) extending the validity of this technique to this power/current rating and 2) as an alternative identification methodology not requiring a regenerative load drive of this size.

Finally, the flux maps measured in self-commissioning were adopted for calibrating a sensorless control strategy. For this kind of applications, a position transducer (usually a resolver) is always embedded in the machine. Anyway, the high safety constrains impose that a back-up sensorless algorithm must always be ready to work in case of resolver failure.

II. SyR Machine Model

The SyR machine is modeled in rotating dq reference frame, where d axis is the rotor direction having the minimum reluctance. The vector quantities are represented as bold lowercase symbols, the matrices as bold uppercase and the scalars as non-bold symbols. The stator voltage is given as:

$$\boldsymbol{v}_{\mathrm{dq}} = R_{\mathrm{s}}\boldsymbol{i}_{\mathrm{dq}} + \frac{\mathrm{d}\boldsymbol{\lambda}_{\mathrm{dq}}}{\mathrm{d}t} + \omega\mathbf{J}\boldsymbol{\lambda}_{\mathrm{dq}} \tag{1}$$

where $\boldsymbol{x}_{\mathrm{dq}} = [x_d\ x_q]^T$ is a vector in dq reference frame, R_{s} is the stator resistance, ω the electrical speed and $\mathbf{J}$ is the imaginary matrix. The machine flux maps are highly non-linear, since the current in both axes contribute to saturate both the flux components (self- and cross-saturation):

$$\begin{cases} \lambda_{\mathrm{d}} &= \lambda_{\mathrm{d}}\left(i_{\mathrm{d}}, i_{\mathrm{q}}\right) \\ \lambda_{\mathrm{q}} &= \lambda_{\mathrm{q}}\left(i_{\mathrm{d}}, i_{\mathrm{q}}\right) \end{cases} \tag{2}$$

The flux maps can be expressed in terms of apparent inductances, which vary with the working point:

$$\boldsymbol{\lambda}_{\mathrm{dq}} = \boldsymbol{L}_{\mathrm{dq}}\boldsymbol{i}_{\mathrm{dq}} = \begin{bmatrix} L_{\mathrm{d}}(i_{\mathrm{d}}, i_{\mathrm{q}}) & 0 \\ 0 & L_{\mathrm{q}}(i_{\mathrm{d}}, i_{\mathrm{q}}) \end{bmatrix} \boldsymbol{i}_{\mathrm{dq}} \tag{3}$$

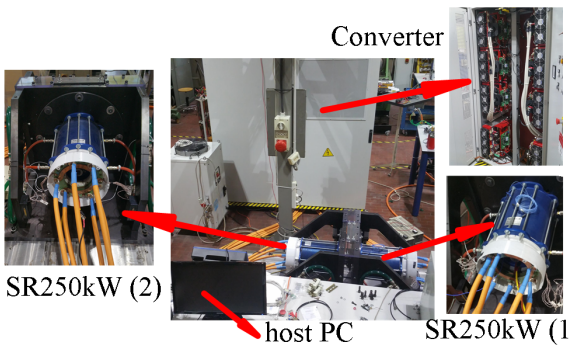

Fig. 1. Experimental setup for testing high current prototype SR250kW.

TABLE I
RATINGS OF THE SR250KW MOTOR PROTOTYPE.

$v_{\rm dc}(V)$	560
Current (A_{RMS})	800 ÷ 1600
Torque (Nm)	190 ÷ 380
Speed (rpm)	12500 ÷ 15000
Power (kW)	250 ÷ 500
Pole pairs	2
Efficiency	0.97
$L_{\rm d}/l_{\rm q}$ (μH)	372 / 30

Finally, the differential inductances are given by the partial derivative of the flux respect to the current:

$$\boldsymbol{l}_{\rm dq} = \begin{bmatrix} l_{\rm d} & l_{\rm dq} \\ l_{\rm qd} & l_{\rm q} \end{bmatrix} = \begin{bmatrix} \frac{\partial \lambda_{\rm d}}{\partial i_{\rm d}} & \frac{\partial \lambda_{\rm d}}{\partial i_{\rm q}} \\ \frac{\partial \lambda_{\rm q}}{\partial i_{\rm d}} & \frac{\partial \lambda_{\rm q}}{\partial i_{\rm q}} \end{bmatrix} \tag{4}$$

III. MOTOR UNDER TEST

Two SR250kW twin motors are mechanically coupled and supplied by a back-to-back 3-phase converter, controlled exploiting a dSpace 1202 PPC controller board. The common DC-link, supplied by a grid connected rectifier, permits the power regeneration between the two machines with reduced energy absorption from the grid. Basically, when one of the machines is working as a motor, thus absorbing relevant power, the other one is generating, so the grid connection must only supply the unavoidable losses present in the system.

The main features of the prototype under test and its power electronic converter are reported in Tables I and II respectively, while Fig. 1 gives an overview of the experimental set-up. The high current rating limits the switching frequency to 5 kHz, while the aeronautic standards impose $v_{\rm dc}$=560 V. Anyway, for the commissioning tests presented here, the $v_{\rm dc}$ was conveniently reduced to 400 V.

IV. COMMISSIONING TEST SEQUENCE

At the time of commissioning, the available FEM model was not yet validated against experimental results, so it was not retained reliable for motor control. This section describes a complete and automatic commissioning procedure adopted for identifying the converter and machine characteristics.

A. Inverter Commissioning

At first, the dependency of the voltage drop across the inverter with the phase current was evaluated. The test sequence [5] was modified and adapted. The motor was current controlled in the stationary $\alpha\beta$ reference frame. At first, i^*_β=300 A was forced to align the rotor, thus avoiding further movements during the rest of the test sequence. Then, i^*_β was increased from zero to 600 A with steps of 5 A, while $i^*_\alpha = 0$.

For each tested current, the corresponding v^*_β was evaluated as the output of the PI controller and normalized, obtaining the $i_\beta - v_\beta$ characteristic shown in Fig. 2(a) (blue dots). The normalization [6] (gain: $\frac{\sqrt{3}}{2}$) permits to obtain the phase voltage drop from β component. As can be seen, this trajectory is almost linear for sufficiently high current. The points having i_β >200 A were interpolated with a straight line (red curve in Fig. 2(a)). The slope of the fitting function gives the aggregate of stator and power modules equivalent ON resistance, evaluated as 3.4 $m\Omega$. Then, the red trajectory was obtained removing this resistive voltage drop from the rough data. This curve represents the non-linear component of the voltage drop across the inverter $V_{th} = \frac{\sqrt{3}}{2} v^*_\beta$, which was stored in form of look-up-table. According to [6], proper inverter compensation is obtained by adding V_{th} to the reference voltage:

$$v^*_{abc} = v_{abc} + V_{th} \cdot sign\,(i_{abc}) \tag{5}$$

It should be noted that [5] adopted a similar test sequence, but the α axis was excited instead of β. The test oriented along β direction permits a better accuracy in the evaluation of the non-linear part of the inverter voltage drop, i.e. for current lower than 150÷200 A [6].

TABLE II
RATINGS OF THE POWER ELECTRONIC CONVERTER.

Power modules	IGBT CM1400DUC-24S
$f_{\rm sw}(kHz)$	5
$v_{\rm dc}(V)$	420÷600
Dead-time (μs)	3.5
Max. current (A)	2800

B. Magnetic Model Self-Commissioning

The machine flux maps were evaluated with self-commissioning test [3]. The goal of this test is double. First, the standard measurement test techniques [2] require a large driving machine, implying a complicate the experimental set-up. Second, the self-commissioning technique [3] resulted accurate for small motors (up to 5-10 kW) but its validity for bigger machines still had to be demonstrated.

In its original formulation [3], the commissioning could be run sensorless. Anyway, every high power machine like

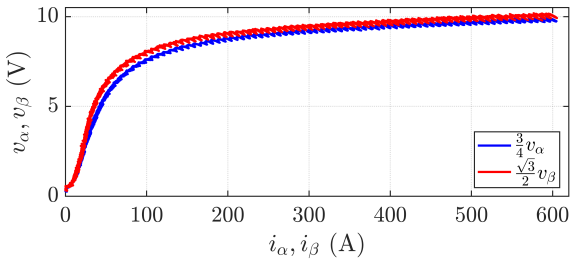

(a)

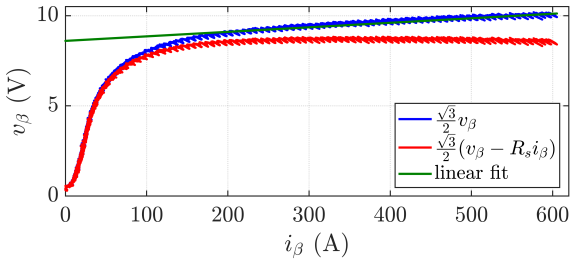

(b)

Fig. 2. Results for inverter commissioning.

SR250kW present a position transducer, and sensorless strategies are required only for fault tolerance reasons. So, in this case the embedded resolver was exploited.

The magnetic model identification is composed by three tests. In **test #1** the d axis is excited with a bipolar square-wave voltage, while i_q is closed loop forced to zero. The polarity of v_d is reversed whenever $|i_\mathrm{d}|$ overcomes a defined threshold value $I_{\mathrm{d,max}}$. Assuming correct voltage reconstruction, the d axis self-saturation characteristic $\lambda_\mathrm{d}(i_\mathrm{d}, i_\mathrm{q}=0)$ is evaluated:

$$\hat{\lambda}_\mathrm{d}\left(i_\mathrm{d}, i_\mathrm{q}\right) = \int v_\mathrm{d}^* - R_\mathrm{s} i_\mathrm{d} dt \tag{6}$$

where R_s is retreaved as in section IV-A. In this test, the motor does not move since torque is not produced, being the d axis only excited. In [7], the same test sequence was adopted but i_q was monitored to detect eventual rotor movement, that would cause test failure in case the commissioning is run sensorless. Basically, the test was stopped if relevant i_q was detected. For this machine, a resolver is adopted, but because of the low phase inductance in case of even minimum position inaccuracy the test may become unstable, since i_q presents high current spikes out of the bandwidth of the PI current control and so relevant torque pulses. Therefore, the automatic stop procedure was maintained.

Then, a dual test is executed for evaluating $\lambda_\mathrm{q}(i_\mathrm{d}=0, i_\mathrm{q})$ (**test #2**). The q axis is square wave voltage excited while i_d is forced to zero. The flux is again estimated from the back-emf:

$$\hat{\lambda}_\mathrm{q}\left(i_\mathrm{d}, i_\mathrm{q}\right) = \int v_\mathrm{q}^* - R_\mathrm{s} i_\mathrm{q} dt \tag{7}$$

Also this test is automatically stopped if a relevant i_d is detected, to avoid instability. Finally, in **test #3** the cross-coupling is evaluated by exciting both the axes with square wave voltages, so the dq plane is explored. The complete flux maps are evaluated using (6),(7). Details can be found in [3].

The voltages and currents during the three tests are reported in Fig. 3. The identification was extended up to i_d=1100 A in test #1 and i_q=1100 A in test #2, while in test #3 the area up to (i_d=700,i_q=400) was explored.

The measurement data were interpolated with an analytical magnetic model [3], permitting to extend the flux maps out of the measurement range and to retrieve the average characteristic from a cloud of measurement points in the dq plane:

$$\hat{i}_\mathrm{d} = \lambda_\mathrm{d}\left(a_{\mathrm{d}0} + a_{\mathrm{dd}}|\lambda_\mathrm{d}|^S + \frac{a_{\mathrm{dq}}}{V+2}|\lambda_\mathrm{d}|^U|\lambda_\mathrm{q}|^{V+2}\right) \tag{8a}$$

$$\hat{i}_\mathrm{q} = \lambda_\mathrm{q}\left(a_{\mathrm{q}0} + a_{\mathrm{qq}}|\lambda_\mathrm{q}|^T + \frac{a_{\mathrm{dq}}}{U+2}|\lambda_\mathrm{d}|^{U+2}|\lambda_\mathrm{q}|^V\right) \tag{8b}$$

This model proved to accurately represent a wide variety of SyR machines in [3], where it was stated that the exponents can be fixed a priori for any SyRMs having low rated power (few kW) or speed (1000 rpm). In this work, its applicability to high speed and power SyRMs is experimentally proved.

According to [7], this self-commissioning test is robust against inaccurate parameters estimation, e.g. R_s and V_th. This robustness is guaranteed by the high test voltage (≈200 V) applied in [3], [7]. In the machine under test the inductances are much lower than in [3], [7], so a lower test voltage (30 V) was applied to guarantee a sufficient number of samples for each current sweep. So, the sensitivity to parameters detuning is higher. Nevertheless, the obtained flux maps resulted very precise, as will be proved in the next section, thanks to the accurate inverter commissioning (Section IV-A).

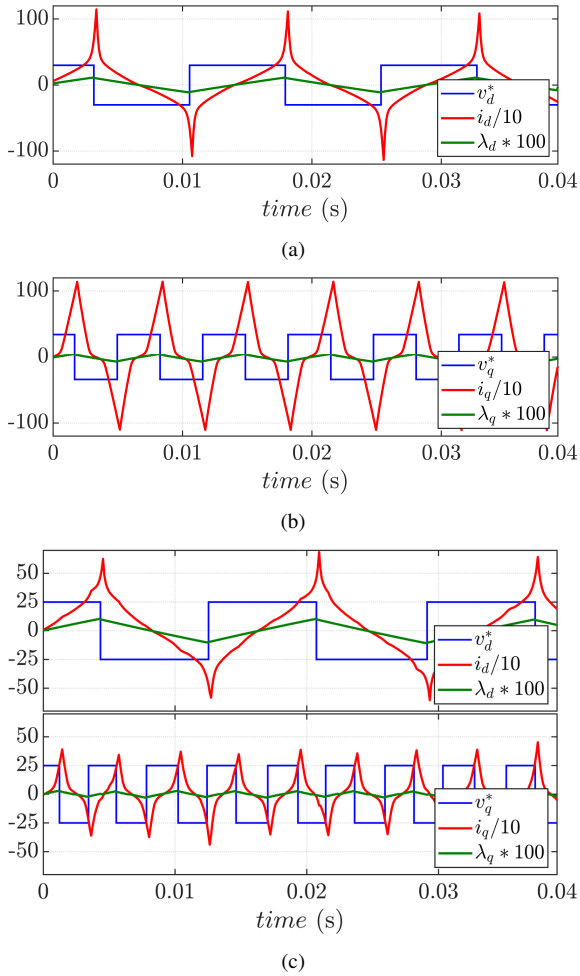

Fig. 3. Voltage, current and estimated flux during self commissioning of the magnetic model. (a) Test #1. (b) Test #2. (c) Test #3.

These flux maps permitted to online estimate the developed torque. Thus, the mechanical inertia (0.047 $kg{\cdot}m^2$) and friction (0.171 Nm) were found by acceleration - deceleration tests.

C. Constant Speed Identification of the Flux Maps

The standard constant speed test [2] was executed to prove the validity of the obtained flux maps. The twin machine imposed a constant speed (1200 rpm), while a proper sequence of current vectors was imposed to the motor under test. Eventual inaccuracies in determining R_s or V_th are compensated using a dedicated motoring-braking-motoring average. Details can be found in [2]. The current plane was explored up to (i_d=850,i_q=1100). Fig. 4 compares the results of the standstill and constant speed tests, showing an almost perfect agreement.

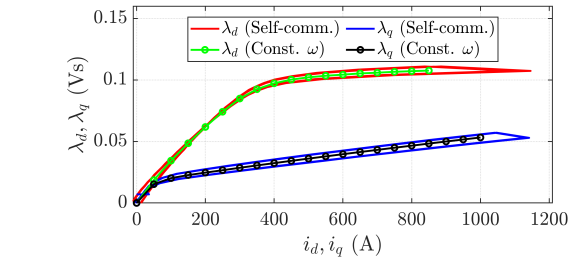

(a)

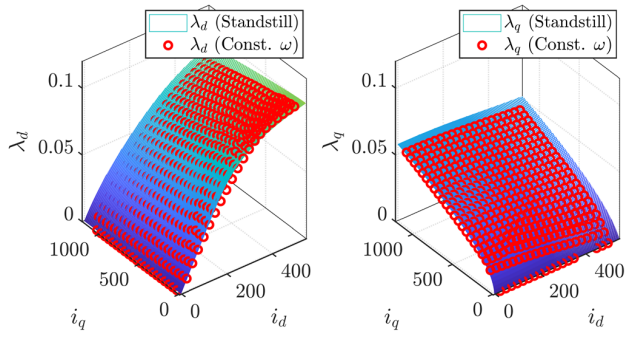

(b)

Fig. 4. Comparison between reference [2] flux maps and standstill self-commissioning. (a) d and q self-saturation. (b) Cross-saturation.

This confirms the validity of both the self-commissioning technique and analytical model for high power prototypes.

D. Harmonic Content Evaluation

In this test, the two motors were run at constant speed and load (4500 rpm, 75 Nm) to evaluate the harmonic content of the back-EMF. The results are shown in Fig. 5.

As can be seen, the motor presents relevant harmonic noise, resulting in high current overshoots not controllable by the PI regulators. In particular, high 6^{th} and 12^{th} harmonics were detected in rotating coordinates, corresponding to the combination of 5^{th}-7^{th} and 11^{th}-13^{th} harmonics in stationary reference frame. This phenomenon strongly limits the operating region of the machine, especially in the speed range. Therefore, at the moment of this work the machine was not tested at the rated power and speed. Several techniques for overcome this problem are under investigation.

V. Sensorless Control

Sensorless control algorithms are usually divided in saliency based and model based methods. The firsts, which can work at low speed or even at standstill, rely on the machine anisotropy:

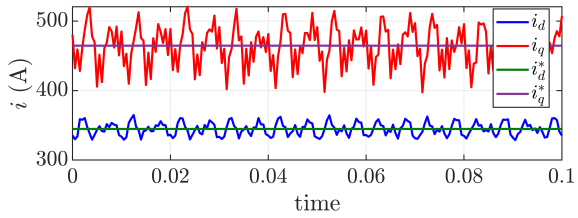

Fig. 5. Steady state speed control test at 4500 rpm and 75 Nm.

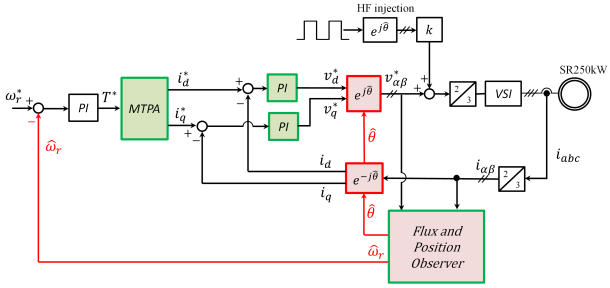

Fig. 6. Block diagram for sensorless control.

a HF signal is injected, and the rotor position $\hat{\theta}$ is tracked by demodulating the HF machine response. Conversely, the latters retrieve $\hat{\theta}$ from manipulations of the motor model. Since this always requires to estimate the back-EMF, model based methods can only work at medium-high speed, where the back-EMF are relevant. In this work, both a saliency based and a model based technique were implemented and tested.

The relevant size of the machine impose several issues to the sensorless control that must be taken into account:

- The current rating imposes low switching frequency (f_{sw}=5 kHz), limiting the position observer bandwidth. The Double Sampling Double Refresh (DSDR) technique virtually increases the switching frequency, but at the cost of higher noise in the current measurement, leading to additional uncertainty in the position estimation.
- This high current also imposes large inverter dead-time, so proper compensation as in Section IV-A is mandatory.
- The commutation of such high current implies high EMI, affecting the current measurement, particularly critical for saliency based sensorless control.
- The low phase inductances introduce the risk of losing the current control in case inappropriate voltage is applied.
- Every SyR machine is almost isotropic for low i_{q}, since the structural ribs are not saturated [8]. This aspect is very critical here since, being the maximum speed 15000 rpm, the ribs are designed thick enough to guarantee sufficient mechanical robustness. So, a relatively high current is necessary to saturate them and the machine is almost isotropic up to $i_{\text{q}} = 80\ A$ (see Fig. 4).

A. Motor Control Scheme

The adopted motor control strategy is based on current vector control in dq rotating coordinates (Fig. 6). The two controlled variables are $i_{\text{d}}, i_{\text{q}}$. At low speed, a HF pulsating voltage is injected along the estimated $\hat{d}$ axis. The parameter k switches on and off this HF injection. Both at low and high speed, a combined flux and position observer retrieves $\hat{\lambda}$, $\hat{T}$, $\hat{\theta}$ and $\hat{\omega}$. The DSDR method was adopted.

B. Saliency Based Position Estimation

At low speed, the sensorless algorithm relies on saliency based position tracking loop. A HF voltage is injected along $\hat{d}$ axis. The low phase inductance suggests to increase as far as possible the injection frequency. This also permits a

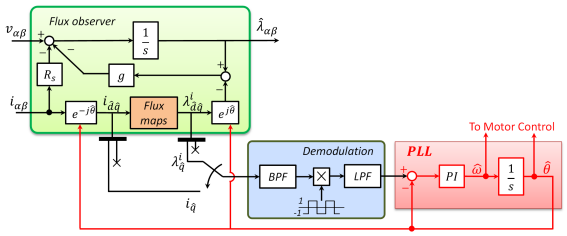

Fig. 7. Flux and position observer for low speed sensorless control.

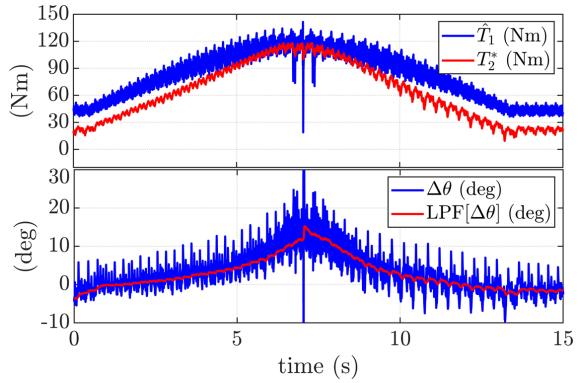

Fig. 8. Sensorless torque control at low speed with demodulation of $i_{\hat{q}}$.

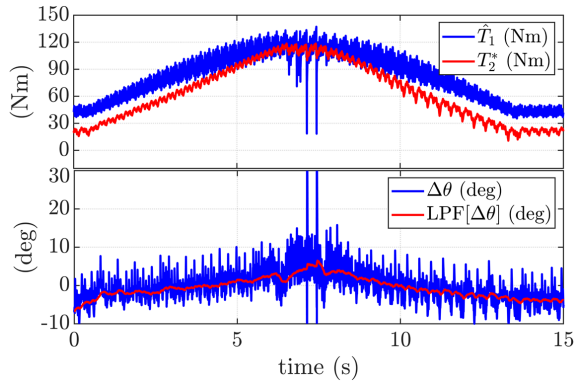

Fig. 9. Sensorless torque control at low speed with demodulation of $\lambda^i_{\hat{q}}$.

better decoupling between fundamental and HF components. Thanks to the DSDR technique, the injection frequency could be pushed up to f_{sw} [9]. Anyway, this method introduces a relevant additional 6^{th} harmonic to the demodulated signal, which already presents a low signal-to-noise ratio for the high EMI disturbances. So, this solution, although possible, was not adopted. A sensorless control similar to [10] was preferred, injecting a pulsating voltage at half of f_{sw}. The injected signal is necessarily a square wave, whose polarity is reversed at every PWM period.

A common saliency based position tracking consists of demodulating the HF current component in q axis, i.e. i_{qh}, whose amplitude is given in [8]. Anyway, that this position tracking loop actually converges to a deviated position [8], with a steady state position error $\Delta\theta_{dq}$ given by:

$$\Delta\theta_{dq} = \frac{1}{2}\arctan\left(\frac{2l_{dq}}{l_d - l_q}\right) \tag{9}$$

A possible method to get rid of the cross-coupling effect is to use the flux estimate in q axis obtained from the current model of the flux observer $\lambda^i_{\hat{q}}$ as position error feedback. The amplitude of its HF component is proportional to $\Delta\theta$:

$$|\lambda^i_{\hat{q}h}| = \frac{u_c\left[l_q\left(l_d - l_q\right) - 2l_{dq}^2\right]}{4\omega_c\left(l_d l_q - l_{dq}^2\right)}\sin\left(2\Delta\theta\right) \approx k'_\epsilon \Delta\theta \tag{10}$$

The flux and position observer adopted at low speed is reported in Fig. 7. A switch permits to choose the signal ($i_{\hat{q}}$ or $\lambda^i_{\hat{q}}$) that is demodulated for position tracking. The two solutions are compared in Fig. 8 and 9, where the motor under test was torque controlled with a slow torque ramp while the twin machine imposed a low speed (100 rpm=0.008 pu). In both cases, $\hat{\theta}$ (and so $\Delta\theta$) is noise due to the high EMI disturbances. A low-pass filtered $\Delta\theta$, not used for motor control, is plotted for better understanding. Fig. 8 presents a relevant position error roughly proportional to the torque, which is considerably reduced when $\lambda^i_{\hat{q}}$ is demodulated (Fig. 9).

C. Model Based Algorithm

When the speed is sufficiently high, so that the back-EMF are reliably evaluated, the HF injection is turned off ($k = 0$ in Fig. 6). The rotor position is retrieved from model based algorithms. The selected method is the Active Flux (AF) concept [8]. The AF vector is defined as:

$$\boldsymbol{\lambda}^{af} = \boldsymbol{\lambda} - L_q \boldsymbol{i} \tag{11}$$

where the stator flux $\boldsymbol{\lambda}$ and current $\boldsymbol{i}$ vectors can be expressed in any reference frame. Using complex representation of the vector quantities $\boldsymbol{X_{dq}} \rightarrow x_d + jx_q$, (11) turns to be:

$$\begin{aligned}\boldsymbol{\lambda}^{af} &= \lambda_d + j\lambda_q - L_q\left(i_d + ji_q\right)\\ &= \left(L_d - L_q\right)i_d\end{aligned} \tag{12}$$

Therefore, the $\boldsymbol{\lambda}^{af}$ vector lies on d axis, as in Fig. 10. The sensorless algorithm consists of computing (11) in $\alpha\beta$ coordinates, and use the direction of $\boldsymbol{\lambda}^{af}$ for defining the d axis orientation. A PLL is added to the AF observer, to improve the robustness of position estimation. Figs. 11 to 13 experimentally validate this model based sensorless control. Fig. 11 is an example of torque control at 1000 rpm (0.077 pu), with a step reference torque (160 Nm). In Figs. 12 and 13, the

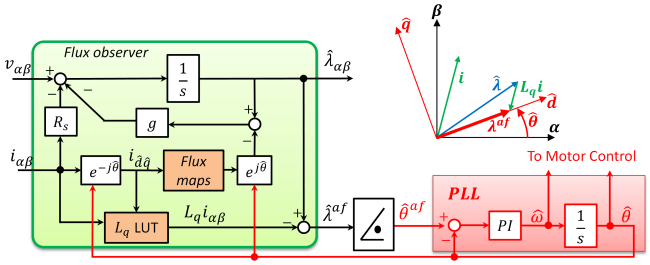

Fig. 10. Flux and position observer based on AF concept.

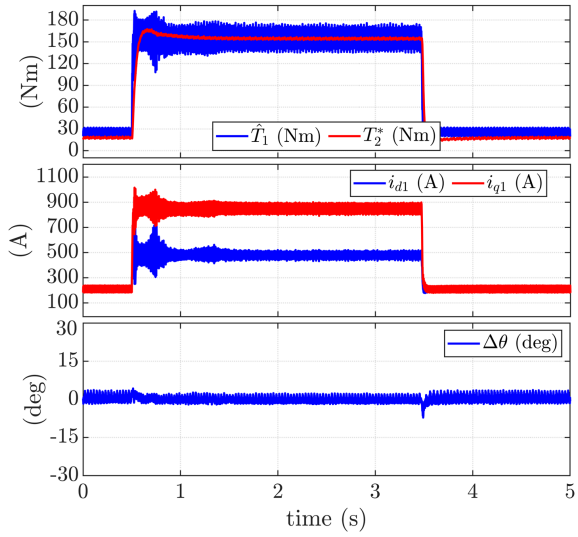

Fig. 11. Sensorless torque control at 1000 rpm (0.077 pu), with step reference T^* to 160 Nm.

motor was speed controlled. Fig. 12 presents the response to a speed reference variation up to 4000 rpm, while a step load (90 Nm) was applied in Fig. 13 with constant reference speed. In each test, the position error is very small even in transient conditions, and the dynamic response is good.

Conclusions

A complete test sequence for a high power SyRM prototype was defined and experimentally verified, including the identification of inverter voltage drop and magnetic model. The size of the machine imposes several constrains and implementation issues that complicates this identification respect to medium-low power drives. All these aspects were addressed and solved. The inverter commissioning resulted accurate enough for a reliable voltage reconstruction during motor commissioning and control. The flux maps retrieved in self-commissioning resulted strictly compatible with the reference. Finally, the obtained inverter characteristic and flux maps were adopted in a sensorless control, working well in every tested conditions.

Acknowledgment

The Authors would like to acknowledge GE-Avio Aero for their support in this research.

References

[1] E. Levi. Multiphase electric machines for variable-speed applications. IEEE Transactions on Industrial Electronics, May 2008.

[2] E. Armando et al., "Experimental Identification of the Magnetic Model of Synchronous Machines," in IEEE Trans. on Ind. App., 2013.

[3] M. Hinkkanen et al. "Sensorless Self-Commissioning of Synchronous Reluctance Motors at Standstill Without Rotor Locking," in IEEE Trans. on Ind. App., 2017.

[4] G. Pellegrino, P. Guglielmi, E. Armando, and R. I. Bojoi, "Self-Commissioning Algorithm for Inverter Nonlinearity Compensation in Sensorless Induction Motor Drives," in IEEE Trans. on Ind. App., 2010.

[5] S. Bolognani and M. Zigliotto, "Self-commissioning compensation of inverter non-idealities for sensorless AC drives applications," *International Conference on Power Electronics, Machines and Drives*, 2002.

[6] P. Pescetto and G. Pellegrino, "Sensorless Standstill Commissioning of Synchronous Reluctance Machines with Automatic Tuning," 2017 IEEE International Electric Machines and Drives Conference (IEMDC), 2017.

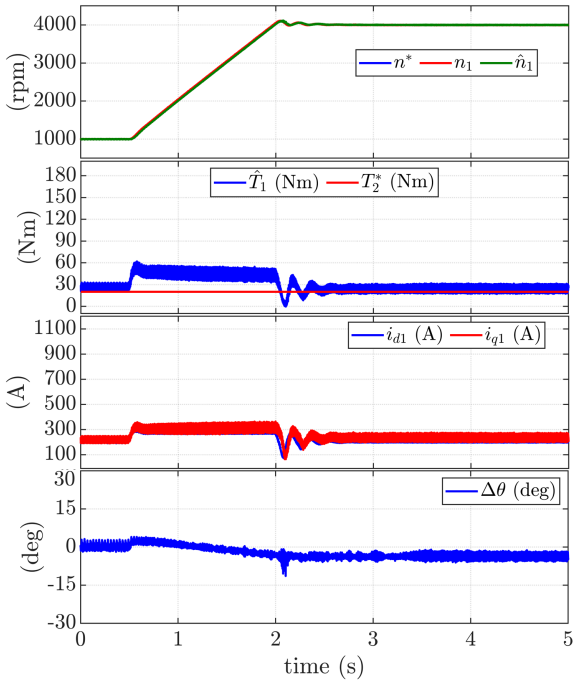

Fig. 12. Sensorless speed control, with step reference from 1000 to 4000 rpm. Load torque: 20 Nm.

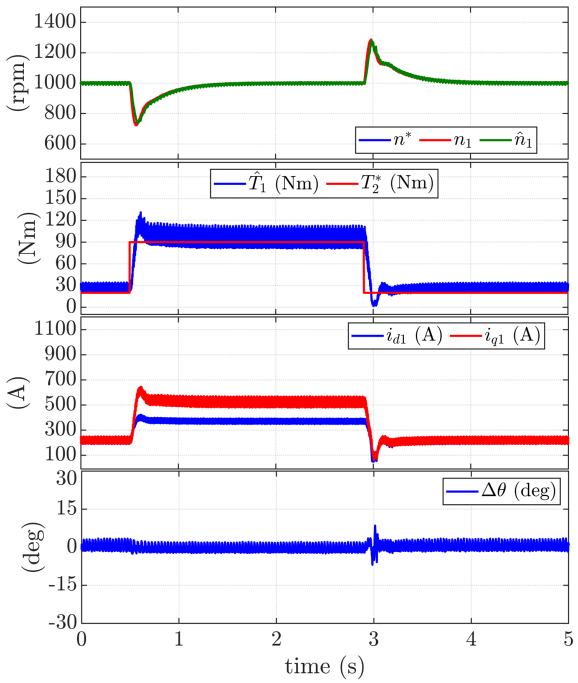

Fig. 13. Sensorless speed control at 1000 rpm (0.077 pu) with step load torque 90 Nm.

[7] A. Yousefi-Talouki et al., "Combined Active Flux and High-Frequency Injection Methods for Sensorless Direct-Flux Vector Control of Synchronous Reluctance Machines," in IEEE Trans. on Power Electr., 2018.

[8] J. M. Liu and Z. Q. Zhu, "Novel Sensorless Control Strategy With Injection of High-Frequency Pulsating Carrier Signal Into Stationary Reference Frame," in IEEE Trans. on Ind. App., 2014.

[9] Y. Yoon, S. Sul, S. Morimoto and K. Ide, "High-Bandwidth Sensorless Algorithm for AC Machines Based on Square-Wave-Type Voltage Injection," in IEEE Transactions on Industry Applications,2011.